

## Article

# Optimization of Crystal Structures in Polyolithionite Concentrate: A Molecular Dynamics Approach to Lithium Extraction Efficiency

María Guadalupe Quezada-Aldaco <sup>1</sup>, Efren Delgado <sup>2</sup>, David Enrique Zazueta-Álvarez <sup>3</sup>,  
Víctor Jesús Martínez-Gómez <sup>1</sup>, Hiram Medrano-Roldán <sup>1</sup>, Perla Guadalupe Vázquez-Ortega <sup>1</sup>,  
Felipe Samuel Hernández-Rodarte <sup>1</sup> and Damián Reyes-Jáquez <sup>1,\*</sup>

- <sup>1</sup> Department of Chemical and Biochemical Engineering, National Technological Institute of Mexico (TecNM)–Durango Institute of Technology (ITD), Blvd. Felipe Pescador 1830, Nueva Vizcaya, Durango 34080, Mexico; 22040317@itdurango.edu.mx (M.G.Q.-A.); v.martinez@itdurango.edu.mx (V.J.M.-G.); hmedrano@itdurango.edu.mx (H.M.-R.); pvazquez@itdurango.edu.mx (P.G.V.-O.); shernandez@itdurango.edu.mx (F.S.H.-R.)
- <sup>2</sup> Food Science and Technology, Department of Family and Consumer Sciences, New Mexico State University, P.O. Box 30001, Las Cruces, NM 88003-8001, USA; edelgad@nmsu.edu
- <sup>3</sup> Ingeniería en Tecnología Ambiental, Universidad Politécnica de Durango, Carretera Durango-México Km 9.5, Durango 34300, Mexico; david.zazueta@unipolidgo.edu.mx
- \* Correspondence: author: damian.reyes@itdurango.edu.mx

**Abstract:** Molecular dynamics (MD) techniques offer significant potential for optimizing mineral extraction processes by simulating economically or physically restrictive conditions at the laboratory level. Lithium, a crucial metal in the electromobility era, exemplifies the need for ongoing re-evaluation of extraction techniques. This research aims to simulate the crystal structures of mineral species present in a polyolithionite mineral concentrate  $[\text{KLi}_2\text{Al}(\text{Si}_4\text{O}_{10})(\text{F},\text{OH})_2]$  using crystallographic data obtained from X-ray diffraction analysis. This study focuses on optimizing these structures, validating them through density comparisons, and determining the interaction parameter between the identified phases and lithium oxide ( $\text{Li}_2\text{O}$ ). The X-ray diffraction analysis revealed five predominant mineral phases: quartz ( $\text{SiO}_2$ ), calcite [ $\text{Ca}(\text{CO}_3)$ ], pyrite ( $\text{FeS}_2$ ), cassiterite ( $\text{SnO}_2$ ), and a compound  $\text{Pb}_6\text{O}_2(\text{BO}_3)_2\text{SO}_4$ . Structural data, including lattice parameters, space groups, and atomic coordinates, were used to construct the crystal structures with Materials Studio 8.0, employing the Crystal Builder module. Optimization was performed using the Forcite module with the Smart optimization algorithm and the Universal force field. The interaction parameter ( $\chi$ ) indicated an affinity between lithium oxide and pyrite, as well as between calcite and quartz.

**Keywords:** mining; geometric optimization; structural validation; miscibility



**Citation:** Quezada-Aldaco, M.G.; Delgado, E.; Zazueta-Álvarez, D.E.; Martínez-Gómez, V.J.; Medrano-Roldán, H.; Vázquez-Ortega, P.G.; Hernández-Rodarte, F.S.; Reyes-Jáquez, D. Optimization of Crystal Structures in Polyolithionite Concentrate: A Molecular Dynamics Approach to Lithium Extraction Efficiency. *Nanomaterials* **2024**, *14*, 1713. <https://doi.org/10.3390/nano14211713>

Academic Editors: Luis Alberto Ruiz Pestana, Wenjie Xia, Zhaoxu Meng and James Evans

Received: 20 September 2024

Revised: 22 October 2024

Accepted: 24 October 2024

Published: 27 October 2024



**Copyright:** © 2024 by the authors. Licensee MDPI, Basel, Switzerland. This article is an open access article distributed under the terms and conditions of the Creative Commons Attribution (CC BY) license (<https://creativecommons.org/licenses/by/4.0/>).

## 1. Introduction

Molecular dynamics (MD) simulation techniques have become essential tools in research across various fields, including biomolecules, polymers, minerals, and other compounds. These techniques are used to test theoretical models and predict experimental behaviors such as interactions and structural dynamics. By describing variations in positions, velocities, and orientations of molecules over time, MD simulations facilitate a deeper understanding of these systems [1,2].

When implementing MD simulations, researchers often rely on complementary analytical techniques to enhance accuracy and efficiency. Techniques such as X-ray crystallography [3], electron microscopy [4], nuclear magnetic resonance (NMR) [5], and electron paramagnetic resonance (EPR) are commonly used to support and refine simulation results [2].

In the mining industry, MD simulations have diverse applications. They can aid in the development of new compounds and structures and simulate interactions between minerals to assess the stability of molecular complexes under varying pressure and temperature conditions [6]. MD simulations can also evaluate the behavior of compounds or crystalline structures under different pressures [7] and determine formation energies at various temperatures [8]. By simulating laboratory conditions that might be challenging to replicate experimentally due to economic or physical constraints, MD techniques offer valuable insights [9].

In recent decades, focus has shifted towards exploring compounds and elements that can aid in the decarbonization of energy sources and address current energy demands. Energy storage and production technologies, such as rechargeable batteries [10], electric vehicles [11], and storage cells [12], are key areas of exploration. Elements like lithium, cobalt, zinc, and magnesium are being investigated as crucial components of energy transition [13].

Mining companies are becoming increasingly interested in developing sustainable technologies to reduce the environmental impact of mineral extraction. Biohydrometallurgy, a branch of biotechnology, explores the economic potential of microbial interactions with mineral compounds while addressing environmental concerns [14]. Molecular dynamics simulations might enhance the efficiency of mineral extraction processes by generating predictive models for ore deposits and optimizing biotechnological treatments [13].

This research focused on simulating the crystalline structures of mineral species present in lithium concentrate from Bacanora Minerals, located in Bacadehuachi, Sonora, Mexico. This study aimed to optimize these structures using X-ray diffraction (XRD) analysis, allowing for a comparison between simulated structural approximations and those observed in the mineral concentrate. Additionally, this research assessed the miscibility parameters between the phases identified through XRD analysis and lithium oxide ( $\text{Li}_2\text{O}$ ) to evaluate their affinity. This research could serve as a foundation for *in silico* evaluations that might otherwise be economically prohibitive, offering significant benefits to the mining industry and related lithium sectors.

## 2. Materials and Methods

### 2.1. Materials

The lithium-bearing mineral concentrate was a clay mineral identified as polyolithionite  $[\text{KLi}_2\text{Al}(\text{Si}_4\text{O}_{10})(\text{F},\text{OH})_2]$  [15]. This material was supplied by Bacanora Minerals, a company located in Sonora, northeastern Mexico, approximately 11 km south of Bacadehuachi, 180 km northeast of Hermosillo, and about 170 km south of the US–Mexico border.

### 2.2. Methods

#### 2.2.1. X-Ray Diffraction Analysis

The morphology of the mineral concentrate was assessed using X-ray diffraction (XRD) analysis. The sample was crushed and sieved to obtain particles smaller than 200 mesh. It was then homogenized to ensure uniform exposure to the X-ray beam. A Rigaku Miniflex 600 X-ray (Rigaku Corp., Tokyo, Japan) diffractometer was used, operating at room temperature with a monochromatic  $\text{Cu K}\alpha$  radiation source ( $\lambda = 0.154$  nm). The analysis was conducted in stepped scan mode with a  $2\theta$  angular range of  $5\text{--}90^\circ$  and a step size of  $0.02^\circ$ .

#### 2.2.2. Crystal Builder

To construct the crystal structures present in the mineral concentrate, we used the Crystal Builder module of Materials Studio 8.0. This involved inputting structural parameters derived from the XRD analysis, such as lattice parameters, space groups, angles, and the coordinates of the constituent atoms for each crystal phase.

### 2.2.3. Geometry Optimization

Geometric optimization of each structure was performed through an energetic evaluation and conformational adjustment. Atomic coordinates and cell parameters were refined until the structure reached its minimum energy state. This was accomplished using the Forcite module [16] with the Smart optimization algorithm [17], which combines various geometry optimization methods to better approximate minimum energy potential. The Universal force field, which incorporates rules based on hybridization and connectivity, was used to calculate forces on atoms from their potential energy. This force field is suitable for complex metallic compounds and predicts geometries and conformational energy differences while considering the crystalline nature of the sample [18].

### 2.2.4. Structural Validation

Structural validation of the crystals involved comparing the densities of simulated structures with those obtained experimentally. Structural densities are closely related to intermolecular optimizations [19,20]; a higher percentage of agreement indicates greater structural accuracy [21,22]. Experimental densities were obtained from X-ray diffraction analysis, while simulated densities were calculated using Materials Studio 8.0. The percentage of agreement between experimental and simulated densities was then computed.

### 2.2.5. Miscibility

An atomic absorption analysis previously conducted on the mineral concentrate samples revealed a lithium concentration of 0.0052%. Given this concentration, lithium oxide was not detected among most species in the X-ray diffraction analysis, as the equipment requires a minimum concentration of 0.5% lithium. Therefore, we employed dynamic simulation techniques to identify the likely predominant entity or species responsible for lithium release. This was carried out using the Blends module of Materials Studio 8.0, which considers the miscibility parameter. The Blends module uses the Flory–Huggins model, a well-known theory of the thermodynamics of mixing and phase separation in binary systems [23]. The general expression for the free energy of mixing is given by Equation (1) [24].

$$\frac{\Delta G}{RT} = \frac{\varnothing_b}{n_b} \ln \varnothing_b + \frac{\varnothing_s}{n_s} \ln \varnothing_s + \chi \varnothing_b \varnothing_s \quad (1)$$

where

$\Delta G$  = Free energy of mixing per mole  $\left(\frac{\Delta G}{mol}\right)$ .

$\varnothing_i$  = Volume fraction of component  $i$ .

$n_i$  = Degree of polymerization of component  $i$ .

$\chi$  = Interaction parameter.

$T$  = Absolute temperature (K).

$R$  = Universal gas constant  $\left(\frac{J}{mol \cdot K}\right)$ .

In the model, the first term represents the combinatorial entropy of the system. This term is typically negative, which favors the formation of a mixed state in pure compounds. A more negative combinatorial entropy value indicates a stronger attraction between the interacting elements as they form a complex [25].

Conversely, the last term represents the free energy of mixing resulting from the interaction. If the interaction parameter,  $\chi$ , is positive, it disfavors the mixed state due to the degrees of freedom and the restricted miscibility of the elements in the mixing complex, which tend to segregate [25]. The interaction parameter ( $\chi$ ) is defined by Equation (2).

$$\chi = \frac{E_{mix}}{RT} \quad (2)$$

where  $E_{mix}$  = mixing energy, i.e., the difference in free energy for the interaction between the mixed state and the pure state.

In the traditional Flory–Huggins model, each mixing component occupies a lattice site. In such a lattice with a coordination number  $Z$ , binding energy represents the interaction energy between two components. This interaction energy allows for the calculation of mixing energy, the interaction parameter  $\chi$ , and the construction of phase diagrams [25]. Mixing energy is described by Equation (3).

$$E_{mix} = \frac{1}{2}Z(E_{bs} + E_{sb} - E_{bb} - E_{ss}) \quad (3)$$

where  $E_{ij}$  ( $E_{bs}$ ,  $E_{sb}$ ,  $E_{bb}$ ,  $E_{ss}$ ) represent the binding energy between a unit of the component and a unit of the component  $i$  and a unit of the component  $j$ .

On the other hand, the Blends module generates multiple molecular orientations by calculating the interaction energy for each configuration. These orientations are classified based on their assigned roles, which are termed the “base role” and “screen role.” There are four possible combinations of these roles, each with an associated binding energy value: base–base ( $E_{bb}$ ), screen–screen ( $E_{ss}$ ), screen–base ( $E_{sb}$ ), and base–screen ( $E_{bs}$ ) [26]. The mixing energy at a given temperature is represented by Equation (4).

$$E_{mix} = \frac{1}{2}(Z_{bs}\langle E_{bs} \rangle_T + Z_{sb}\langle E_{sb} \rangle_T - Z_{ss}\langle E_{ss} \rangle_T) \quad (4)$$

A value of  $\chi \leq 0$  indicates that, at a given temperature, the molecules interact favorably, allowing the mixture to potentially exhibit a single phase. Conversely, if  $\chi \geq 0$ , it suggests that the molecules have a preference for being surrounded by similar components rather than mixing. Finally, if  $\chi \gg 0$ , this indicates that the contribution to free energy surpasses the combinatorial entropy of the mixture, leading to phase separation into two distinct phases.

### 3. Results

#### 3.1. X-Ray Diffraction Analysis

The results of the XRD analysis are shown in Figure 1. The data reveal the presence of five predominant species. According to the quantitative Rietveld analysis (RIR) performed by the equipment, the most abundant compound is quartz ( $\text{SiO}_2$ ), constituting 92% of the sample. This is followed by calcite [ $\text{Ca}(\text{CO}_3)$ ], at 5.4%. Additionally, the analysis identified pyrite ( $\text{FeS}_2$ ), tin oxide ( $\text{SnO}_2$ ), and a compound with the formula  $\text{Pb}_6\text{O}_2(\text{BO}_3)_2\text{SO}_4$ .

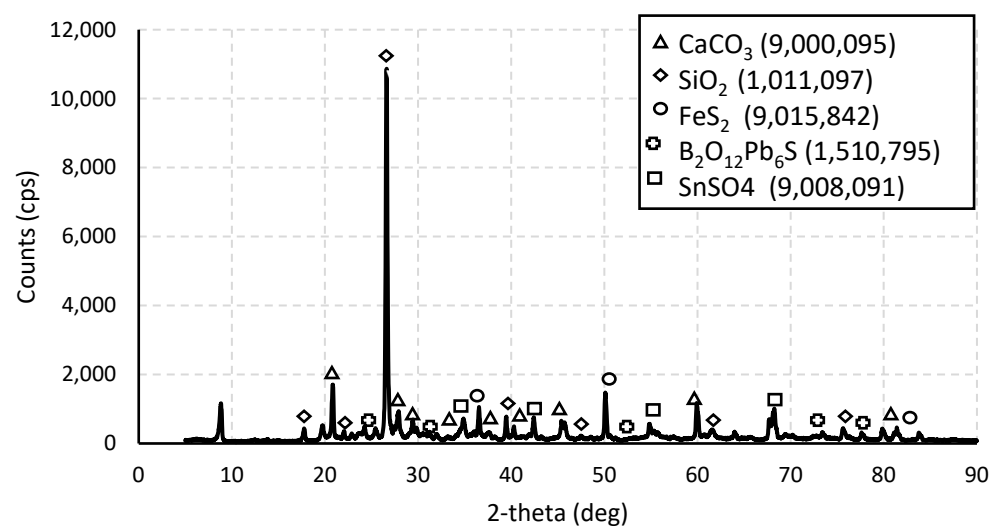


Figure 1. Diffraction pattern of the mineral sample with lithium and its majority species.

### 3.2. Crystal Builder

The XRD analysis provided crystallographic data, including space groups, lattice parameters (Table 1), and atomic positions within the crystal lattice (Table 2). This information was utilized to construct crystals using the Crystal Builder module in Materials Studio 8.0 software.

**Table 1.** Crystallographic information obtained from XRD analysis of lithium-bearing mineral concentrate.

Phase	Formula	Space Group	Lattice Parameters					
			a (Å)	b (Å)	c (Å)	$\alpha$ (°)	$\beta$ (°)	$\gamma$ (°)
Calcite	CaCO <sub>3</sub>	167: R-3c	4.9937	4.9937	17.0792	90	90	120
Quartz	SiO <sub>2</sub>	152: P3121	4.9198	4.9198	5.4018	90	90	120
Pyrite	FeS <sub>2</sub>	205: Pa-3	5.4279	5.4279	5.4279	90	90	90
Pb <sub>6</sub> O <sub>2</sub> (BO <sub>3</sub> ) <sub>2</sub> SO <sub>4</sub>	B <sub>2</sub> O <sub>12</sub> Pb <sub>6</sub> S	62: Pnma	6.3849	11.3296	17.7568	90	90	90
Tin oxide	SnSO <sub>4</sub>	62: Pnma	8.6952	5.3834	6.9650	90	90	90
Lithium Oxide *	LiO <sub>2</sub>	Fm $\bar{3}$ m	4.65	4.65	4.65	90	90	90

\* Information obtained from the database The Materials Project (2020) [27].

**Table 2.** Structural parameters corresponding to the atomic coordinates for each of the phases obtained in the XRD analysis.

Phase	Element	X	Y	Z
Calcite (CaCO <sub>3</sub> )	Ca	0.000	0.000	0.000
	C	0.000	0.000	0.250
	O	0.257	0.000	0.250
Quartz (SiO <sub>2</sub> )	Si	0.465	0.000	0.333
	O	0.417	0.278	0.222
Pyrite (FeS <sub>2</sub> )	Fe	0.000	0.000	0.333
	S	0.625	0.625	0.625
	O	0.030	0.025	0.447
	S	0.212	0.250	0.493
	O	0.167	0.650	0.974
	O	0.087	0.250	0.161
	Pb	0.224	0.250	0.292
	Pb	0.171	0.093	0.105
Pb <sub>6</sub> O <sub>2</sub> (BO <sub>3</sub> ) <sub>2</sub> SO <sub>4</sub>	O	0.164	0.250	0.571
	Pb	0.402	0.250	0.699
	B	0.079	0.508	0.748
	O	0.141	0.597	0.718
	Pb	0.645	0.590	0.102
	O	0.750	0.491	0.829
	O	0.281	0.750	0.355
	O	0.024	0.402	0.713
	Sn	0.208	0.250	0.222
	S	0.069	0.250	0.694
Tin sulfate (O <sub>4</sub> SSn)	O	-0.083	0.250	0.597
	O	0.194	0.250	0.550
	O	0.088	0.020	0.819
Lithium Oxide (Li <sub>2</sub> O)	O	0.000	0.000	0.000
	Li	0.250	0.750	0.250

The first step in constructing the crystals was defining the unit cell, starting with the information provided by the XRD analysis on lattice parameters, including size and corresponding angles [28] (Table 1, Figure 2). Next, the coordinates of the atoms were inputted to specify their positions within the cell (Table 2). For the creation of the lithium oxide ( $\text{Li}_2\text{O}$ ) crystal, structural data such as lattice parameters, space groups, and atomic coordinates were obtained from The “Materials Project” database [27].

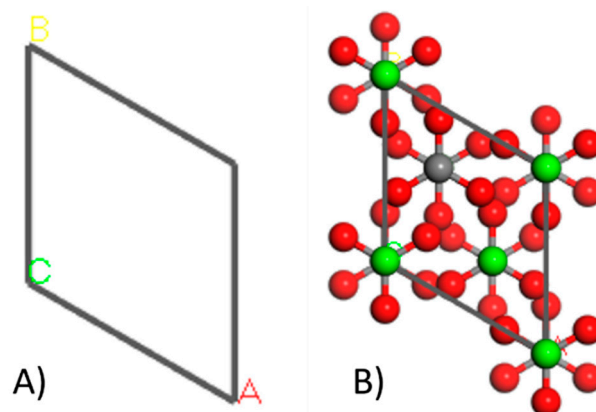


**Figure 2.** Representation of the unit cell corresponding to the construction of a calcite crystal (A) and representation of the calcite crystal after adding the atoms in the indicated positions (B).

### 3.3. Geometry Optimization

Geometry optimization was carried out using the Forcite module, employing the Smart optimization algorithm and the Universal force field. This process enabled us to achieve the structures in their minimum energy state. Figures 3 and 4 illustrate the structures before and after geometry optimization, highlighting differences in atomic size and arrangement.

The Universal force field (UFF) has been widely utilized in molecular dynamics (MD) simulations across various studies involving inorganic compounds, demonstrating its validity and reliability in computational modeling. The UFF is particularly advantageous due to its ability to provide a consistent framework for simulating a diverse range of materials, including metal–organic frameworks (MOFs) and other inorganic structures.

For instance, [29] conducted MD simulations using the UFF within the Forcite module of Materials Studio to investigate the growth limits of ZIF-8 thin films. Their work involved constructing defect-free models based on X-ray crystal structures, showcasing the UFF’s capability to accurately represent the structural properties of complex inorganic materials [29]. Similarly, [30] employed the UFF to calculate vibrational frequencies and temperatures of rhodochrosite crystals, further validating the method’s effectiveness in predicting the physical properties of inorganic compounds.

Moreover, the UFF has been successfully applied in studies focusing on gas separation processes. The authors of [31] utilized the UFF in their MD simulations to explore the efficiency of helium separation using a two-dimensional metal–organic framework, demonstrating the force field’s applicability in practical scenarios involving gas interactions. Additionally, [32] highlighted the importance of selecting appropriate force fields for MOFs, comparing the UFF with other generic force fields and finding it to yield reliable predictions for  $\text{CO}_2$  separation processes.

The versatility of the UFF is further illustrated by its application in various other studies. For example, Aly et al. optimized the molecular structures of metal complexes using the UFF, confirming its utility in quantum chemical studies [33]. In another study, [34] employed the UFF to simulate the behavior of polyether/polyamide-Ag membranes for pollutant capture, reinforcing the method’s robustness in modeling interactions in complex systems.

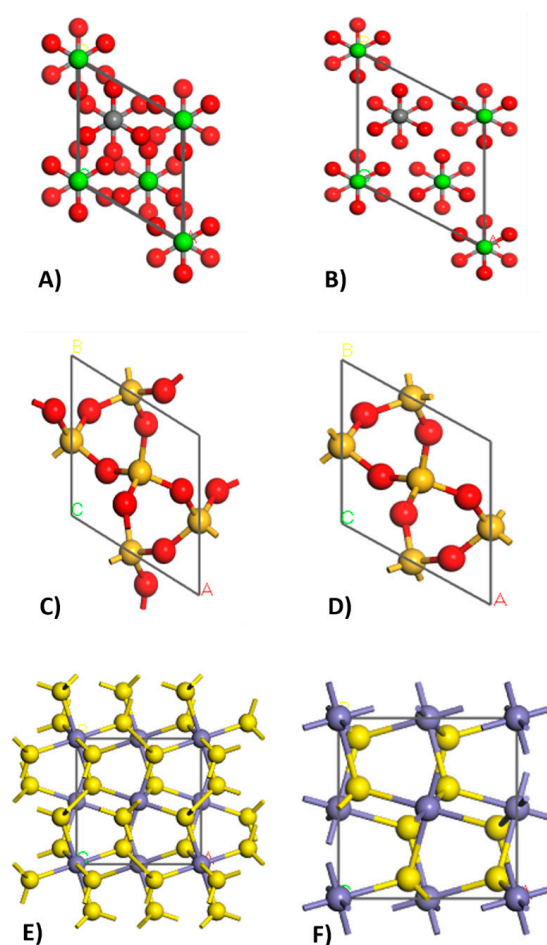


**Figure 3.** Simulated structures before geometric optimization with an initial enthalpy of 2780.34 kcal/mol to calcite (A), 19.79 kcal/mol to quartz (C), and 475.62 kcal/mol to pyrite (E); and simulated structures after geometric optimization with a final enthalpy of 81.39 kcal/mol to calcite (B),  $-28.03$  kcal/mol to quartz (D), and 368.69 kcal/mol to pyrite (F).

The UFF has demonstrated significant reliability in predicting inorganic crystal structures, particularly when benchmarked against specialized force fields. For instance, Addicoat et al. showed that Universal force field for metal–organic frameworks (UFF4MOF) parameters yield lattice parameters for MOFs comparable to those derived from dedicated force fields, indicating the UFF’s robustness in this domain [35]. Furthermore, Jailliet et al. emphasized the UFF’s versatility, as it encompasses parameterizations for all elements up to atomic number 103, making it applicable across a wide range of inorganic systems [36]. This adaptability is crucial for modeling complex interactions in materials science, as evidenced by its successful application in various studies, including those on metal complexes [36]. Additionally, the accuracy of UFF computations has been validated through comparisons with experimental data, reinforcing its utility in computational modeling of crystal structures [37]. Overall, the UFF’s comprehensive parameterization and proven performance in diverse applications underscore its value in predicting inorganic crystal structures reliably. In summary, the UFF has been validated through multiple studies that demonstrate its effectiveness in simulating the molecular dynamics of inorganic compounds and materials. Its consistent performance across diverse applications underscores its relevance in computational materials science.

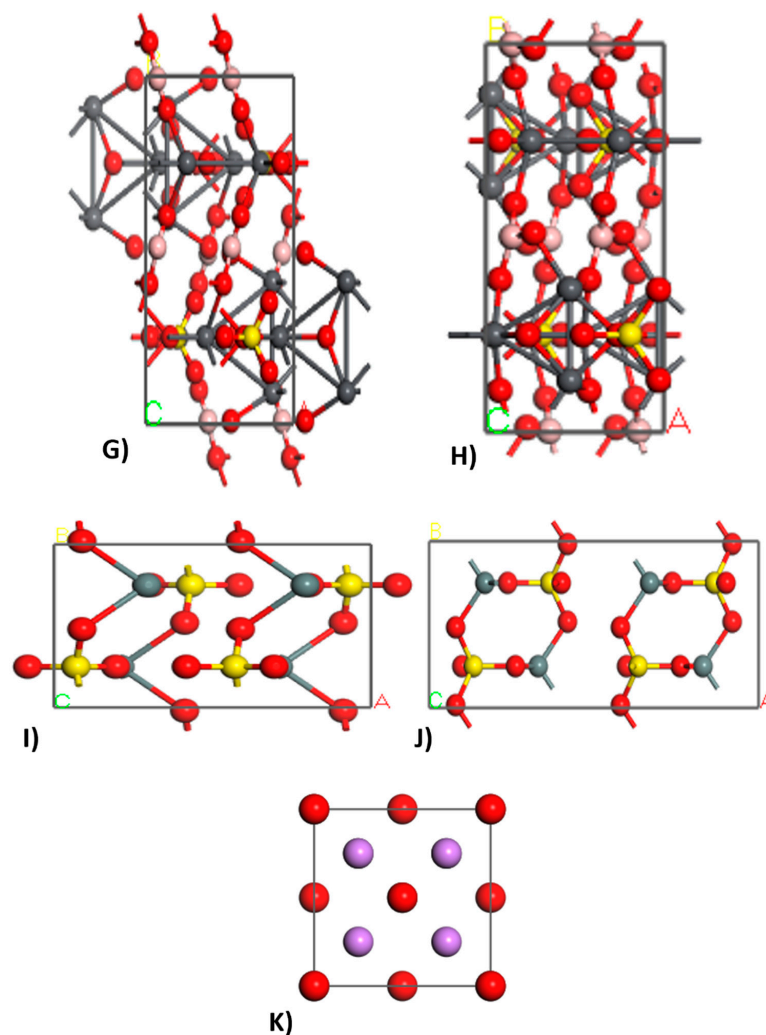


**Figure 4.** Simulated structures before geometric optimization with an initial enthalpy of 11867.75 kcal/mol to  $\text{Pb}_6\text{O}_2(\text{BO}_3)_2\text{SO}_4$  (G), 11867.75 kcal/mol to tin sulfate (I), and 81.78 kcal/mol to lithium oxide (K); and simulated structures after geometric optimization with a final enthalpy of 5466.76 kcal/mol to  $\text{Pb}_6\text{O}_2(\text{BO}_3)_2\text{SO}_4$  (H), and 5466.76 kcal/mol to tin sulfate (J).

### 3.4. Structural Validation

Table 3 presents the structural validation for the optimized figures by density comparison, where coincidence can be observed for five of the six simulated structures, except for calcite.

**Table 3.** Structural validation of the optimized figures by density comparison.

Name	Formula	Density [g/cm <sup>3</sup> ]	
		Experimental	Simulated
Calcite	$\text{CaCO}_3$	2.703	1.697
Quartz	$\text{SiO}_2$	2.643	2.708
Pyrite	$\text{FeS}_2$	4.983	4.594
$\text{Pb}_6\text{O}_2(\text{BO}_3)_2\text{SO}_4$	$\text{B}_2\text{O}_{12}\text{Pb}_6\text{S}$	7.699	6.330
Tin sulfate	$\text{SnSO}_4$	4.375	3.540
Lithium oxide	$\text{LiO}_2$	1.960	1.959

Errors in calculated densities, both experimental and simulation-based, can arise from several factors. For experimental densities obtained through X-ray diffraction, inaccuracies may stem from instrumental calibration, sample purity, and environmental conditions during measurement, which can affect the precision of density values [38]. Additionally, the presence of defects or imperfections in the crystal structure can lead to discrepancies between measured and theoretical densities.

In simulation-based density calculations, such as those performed using Materials Studio, errors can occur due to the choice of computational parameters, including the level of theory, basis set, and optimization algorithms used [39]. Furthermore, approximations inherent in the models, such as the generalized gradient approximation (GGA) in density functional theory, can lead to systematic errors in predicted densities [40]. Assumptions made regarding intermolecular interactions and simplifications in the simulation models can also contribute to inaccuracies [41]. Overall, a comprehensive understanding of both experimental and computational limitations is essential for interpreting density results accurately.

### 3.5. Interaction Parameter

The interaction parameter ( $\chi$ ) was evaluated, and was taken as the basis on which the miscibility of each of the simulated crystals would be evaluated, with lithium oxide as a screen, thus obtaining the miscibility parameters presented in Table 4.

**Table 4.** Interaction parameter  $\chi$  (Chi) for Li<sub>2</sub>O for each simulated crystal.

Base	Display	$\chi$
Pb <sub>6</sub> O <sub>2</sub> (BO <sub>3</sub> ) <sub>2</sub> SO <sub>4</sub>	LiO <sub>2</sub>	67.4689
Tin sulfate	LiO <sub>2</sub>	11.1287
Quartz	LiO <sub>2</sub>	8.9556
Calcite	LiO <sub>2</sub>	4.2978
Pyrite	LiO <sub>2</sub>	0.6052

The Flory–Huggins interaction parameter  $\chi$  can be related to the Hildebrand solubility parameter  $\delta$  and expressed as a function of temperature. A small value of  $\chi$  is generally an indicator of miscibility in a binary system [42].

## 4. Discussion

Geometric optimization, which involves reducing cell sizes and adjusting atomic arrangements, led to a significant decrease in the system's specific enthalpy. For calcite, this change was from an initial enthalpy of 2780.34 kcal/mol (A) to a final enthalpy of 81.39 kcal/mol (B). Geometric optimization was conducted for each simulated crystal, as shown in Figures 3 and 4. However, the simulated crystal for lithium oxide (K) was not geometrically optimized because the data from the database already represent the ideal crystal structure for that compound in its minimum energy state [43–45].

The differences observed in structural validation for the optimized figures, as measured by density comparisons, may stem from the optimization process, which includes two main stages: energy evaluation and conformation adjustment. In the energy evaluation stage, conformations and energy terms are assessed and defined. The conformation adjustment stage aims to reduce energy expression, which may be achieved through adjustment or require additional iterations. The efficiency of the optimization is determined by both the time taken to evaluate the energy expression and the number of iterations needed to reach the minimum energy state [46]. Although two full simulations were performed for each structure, no significant change in structural density was observed. To achieve the minimum energy state, it may be necessary to increase the number of iterations or vary the force field.

The interaction parameter  $\chi \geq 0$  indicates a tendency for components to remain separate without mixing, as seen with the lowest values in interactions between pyrite and lithium oxide (0.6052), calcite (4.2978), and quartz (8.9556). Conversely, an  $\chi \gg 0$  value suggests phase separation in the mixture, as observed for the  $\text{Pb}_6\text{O}_2(\text{BO}_3)_2\text{SO}_4$  compound.

In molecular dynamics simulations conducted using Materials Studio, the values of binding energies and coordination numbers (Z) are derived through a combination of computational techniques and modules available within the software. The binding energy, which quantifies the stability of a molecular system, is typically calculated using density functional theory (DFT) or force field methods. For instance, the DMol3 module in Materials Studio is frequently employed to perform DFT calculations, allowing researchers to obtain total energies and electronic properties essential for determining binding energies [47,48].

Coordination numbers, which indicate the number of nearest neighbors surrounding a central atom, are often derived from the analysis of radial distribution functions (RDFs) obtained during MD simulations. The Forcite module in Materials Studio is particularly useful for such calculations, as it allows for the simulation of molecular interactions and the extraction of structural information from the resulting trajectories [49]. By analyzing the RDF, one can determine the peak positions corresponding to the distances of nearest neighbors, which directly informs the coordination number [50]. This approach has been validated in various studies, where MD simulations have successfully modeled the solvation shells and coordination environments of ions in different solvents [50].

Furthermore, the integration of these computational techniques with advanced visualization tools in Materials Studio enhances our understanding of material properties at the atomic level. For example, the CASTEP module can be utilized for geometry optimization and electronic structure calculations, which are crucial for accurately determining both binding energies and coordination numbers in complex materials [51,52]. The combination of these methodologies allows researchers to comprehensively analyze interactions within materials, leading to insights into their mechanical and thermal properties [53].

In summary, the determination of binding energies and coordination numbers in molecular dynamics simulations using Materials Studio involves a multifaceted approach that leverages DFT calculations, force field methods, and detailed structural analysis of simulation data. This integrated methodology provides a robust framework for exploring the intricate behaviors of materials at the molecular level.

## 5. Conclusions

In conclusion, the application of molecular dynamics (MD) simulations in this study is strongly supported by key quantitative characteristics that enhance our understanding of mineral extraction processes, particularly for lithium. The identification of five mineral phases—quartz, calcite, pyrite, tin oxide, and  $\text{Pb}_6\text{O}_2(\text{BO}_3)_2\text{SO}_4$ —highlights the complexity of the polyolithionite mineral concentrate, necessitating detailed MD simulations to model their interactions. Structural optimization through precise crystallographic data, including lattice parameters and atomic coordinates, enables reliable predictions of phase behavior. Additionally, the validation of optimized structures via density comparisons provides a critical benchmark for assessing thermodynamic properties. The calculated miscibility parameters ( $\chi$ ) further illustrate significant affinities between lithium oxide and pyrite, as well as between calcite and quartz, offering valuable insights for optimizing extraction pathways. These findings collectively underscore the importance of MD simulations in advancing sustainable lithium extraction methodologies in the context of the electromobility era.

**Author Contributions:** Conceptualization, D.R.-J.; Data curation, P.G.V.-O.; Formal analysis, V.J.M.-G.; Funding acquisition, E.D.; Investigation, M.G.Q.-A.; Project administration, D.R.-J.; Resources, F.S.H.-R.; Software, V.J.M.-G.; Supervision, D.E.Z.-Á. and H.M.-R.; Writing—original draft, M.G.Q.-A.; Writing—review and editing, D.R.-J. All authors have read and agreed to the published version of the manuscript.

**Funding:** This research received no external funding.

**Data Availability Statement:** The original contributions presented in this study are included in this article. Further inquiries can be directed to the corresponding author.

**Conflicts of Interest:** The authors declare no conflicts of interest.

## References

1. Hollingsworth, S.A.; Dror, R.O. O. Molecular dynamics simulation for all. *Neuron* **2018**, *99*, 1129–1143. [CrossRef] [PubMed]
2. Kozak, F.; Kurzbach, D. How to assess the structural dynamics of transcription factors by integrating sparse NMR and EPR constraints with molecular dynamics simulations. *Comput. Struct. Biotechnol. J.* **2021**, *19*, 2097–2105. [CrossRef] [PubMed]
3. Satoh, M.; Saburi, H.; Tanaka, T.; Matsuura, Y.; Naitow, H.; Shimozone, R.; Yamamoto, N.; Inoue, H.; Nakamura, N.; Yoshizawa, Y.; et al. Multiple binding modes of a small molecule to human Keap1 revealed by X-ray crystallography and molecular dynamics simulation. *FEBS Open Bio.* **2015**, *5*, 557–570. [CrossRef] [PubMed]
4. Rumyantsev, A.V.; Borgardt, N.I.; Prikhodko, A.S.; Chaplygin, Y.A. Characterizing interface structure between crystalline and ion bombarded silicon by transmission electron microscopy and molecular dynamics simulations. *Appl. Surf. Sci.* **2021**, *540*, 148278. [CrossRef]
5. Waller, C.; Marzinek, J.K.; McBurnie, E.; Bond, P.J.; Williamson, P.T.F.; Khalid, S. Impact on *S. aureus* and *E. coli* membranes of treatment with chlorhexidine and alcohol solutions: Insights from molecular simulations and nuclear magnetic resonance. *J. Mol. Biol.* **2023**, *435*, 167953. [CrossRef]
6. Liu, X.; Lu, X.; Wang, R.; Zhou, H.; Xu, S. Speciation of gold in hydrosulphide-rich ore-forming fluids: Insights from first-principles molecular dynamics simulations. *Geochim. Et Cosmochim. Acta* **2011**, *75*, 185–194. [CrossRef]
7. Pagliai, M.; Muniz-Miranda, M.; Cardini, G.; Schettino, V. Raman and infrared spectra of minerals from ab initio molecular dynamics simulations: The spodumene crystal. *J. Mol. Struct.* **2011**, *993*, 151–154. [CrossRef]
8. Xiao, F.; Lin, W.; Cheng, Q. Ab-initio calculations and molecular dynamics simulations of In, Ag, and Cu replacing Zn in sphalerite: Implications for critical metal mineralization. *Ore Geol. Rev.* **2023**, *163*, 105699. [CrossRef]
9. Vargas, K.I.; Medrano, H.; Reyes, D. Comparative study of chemical process and biotechnological process for the removal of bismuth from mining concentrates. *Rev. Mex. De. Ing. Química.* **2021**, *20*, Proc2215. [CrossRef]
10. Li, S.; Hu, M.; Li, Y.; Gong, C. Fractional-order modeling and soc estimation of lithium-ion battery considering capacity loss. *Int. J. Energy Res.* **2018**, *43*, 417–429. [CrossRef]
11. Zhang, Y.; Zhao, C.; Dai, B.; Li, Z. Dynamic simulation of permanent magnet synchronous motor (pmsm) electric vehicle based on simulink. *Energies* **2022**, *15*, 1134. [CrossRef]
12. Zhang, K.; Zhou, G.; Fang, T.; Jiang, K.; Liu, X. Structural reorganization of ionic liquid electrolyte by a rapid charge/discharge circle. *J. Phys. Chem. Lett.* **2021**, *12*, 2273–2278. [CrossRef] [PubMed]
13. Alonso, E.; Álvarez, E.; Blanco, F.; Espi, J.A.; Herrera, J.; Larrea, M.; López, C.; Larrea, M.; Marqués, A.L.; De la Torre, L. Mineral Raw Materials in the Energy Transition and Digitalization. The Role of Mining and Metallurgy. Available online: <https://www.raing.es> (accessed on 2 June 2024).
14. González, E. Bioreduction of Soluble and Insoluble Iron. Available online: <https://eprints.ucm.es/id/eprint/34148/1/T36640> (accessed on 12 May 2024).
15. Alatorre, A.E.; & Santillán, Y. Lithium Deposits. Available online: [https://www.revistageomimet.mx/wp-content/uploads/2020/12/G\\_348.pdf](https://www.revistageomimet.mx/wp-content/uploads/2020/12/G_348.pdf). (accessed on 9 May 2024).
16. Oliveira, A.; Barbosa, M.; Netz, P. Interplay between structure and density anomaly for an isotropic core-softened ramp-like potential. *Phys. A Stat. Mech. Its Appl.* **2007**, *386*, 744–747. [CrossRef]
17. Errington, J.; Debenedetti, P. Relationship between structural order and the anomalies of liquid water. *Nature* **2001**, *409*, 318–321. [CrossRef]
18. Svärd, M.; Rasmuson, Å.C. Force fields and point charges for crystal structure modeling. *Ind. Eng. Chem. Res.* **2009**, *48*, 2899–2912. [CrossRef]
19. Nam, K.H.; Choi, H.K.; Yeo, H.; You, N.H.; Ku, B.C.; Yu, J. Molecular design and property prediction of sterically confined polyimides for thermally stable and transparent materials. *Polymers* **2018**, *10*, 630. [CrossRef]
20. Fereidoon, A.; Aleghaee, S.; Taraghi, I. Mechanical properties of hybrid graphene/TiO<sub>2</sub> (rutile) nanocomposite: A molecular dynamics simulation. *Comput. Mater. Sci.* **2015**, *102*, 220–227. [CrossRef]
21. De la Torre, A.; Reyes, D.; Medrano, H. Molecular Dynamics: An Alternative for the Prediction of Affinity Between Mining Compounds. *Rev. Electrónica ANFEI Digit.* **2021**, *13*. Available online: <http://www.anfei.mx/revista/index.php/revista/article/view/721> (accessed on 20 September 2024).
22. Gupta, J.; Nunes, C.; Vyas, S.; Jonnalagadda, S. Prediction of solubility parameters and miscibility of pharmaceutical compounds by molecular dynamics simulations. *J. Phys. Chem. B* **2011**, *115*, 2014–2023. [CrossRef]
23. Valavi, M.; Ukrainczyk, M.; Dehghani, M.R. Prediction of solubility of active pharmaceutical ingredients by semi-predictive Flory Huggins/Hansen model. *J. Mol. Liquids.* **2017**, *246*, 166–172. [CrossRef]
24. Fuh, A.Y.G.; Huang, K.Y.C. Solubilization of functionalized (5, 5) single-walled carbon nanotubes in 5CB nematic liquid crystals: Simulation using Flory–Huggins theory. *Model. Simul. Mater. Sci. Eng.* **2011**, *19*, 025006. [CrossRef]

25. Anamu, U.S.; Ayodele, O.O.; Olorundaisi, E.; Babalola, B.J.; Odetola, P.I.; Ogunmefun, A.; Ukoba, K.; Jen, T.C.; Olubambi, P.A. Fundamental design strategies for advancing the development of high entropy alloys for thermo-mechanical application: A critical review. *J. Mater. Res. Technol.* **2023**, *27*, 4833–4860. [CrossRef]
26. Cardenal, A.D.; Ramadhar, T.R. The crystalline sponge method: Quantum chemical in silico derivation and analysis of guest binding energies. *CrystEngComm* **2021**, *23*, 7570–7575. [CrossRef]
27. The Materials Project. “Materials Data on Li<sub>2</sub>O by Materials Project”. United States. 2020. Available online: <https://next-gen.materialsproject.org/materials/mp-1960> (accessed on 20 September 2024).
28. Rodríguez, D.; Pámanes, G.; Delgado, E.; Rodríguez, M.D.; Medrano, H.; Reyes, D. Extraction optimization and molecular dynamic simulation of cellulose nanocrystals obtained from bean forage. *Biocatal. Agric. Biotechnol.* **2022**, *43*, 102443. [CrossRef]
29. Perrot, V.; Roussey, A.; Benayad, A.; Veillerot, M.; Mariolle, D.; Solé-Daura, A.; Jousseau, V. Zif-8 thin films by a vapor-phase process: Limits to growth. *Nanoscale* **2023**, *15*, 7115–7125. [CrossRef] [PubMed]
30. Gobato, R. Calculation by uff method of frequencies and vibrational temperatures of the unit cell of the rhodochrosite crystal. *Int. J. Adv. Chem.* **2019**, *7*, 77–81. [CrossRef]
31. Wang, J.; Li, Y.; Yang, Y.; Li, Y.; Zhao, M.; Liu, W.; Qu, Y. Efficient helium separation with two-dimensional metal–organic framework Fe/Ni-PTC: A theoretical study. *Membranes* **2021**, *11*, 927. [CrossRef]
32. Dokur, D.; Keskin, S. Effects of force field selection on the computational ranking of MOFs for CO<sub>2</sub> separations. *Ind. Eng. Chem. Res.* **2018**, *57*, 2298–2309. [CrossRef]
33. Aly, S.; Elganzory, H.; Mahross, M.; Abdalla, E. Quantum chemical studies and effect of gamma irradiation on the spectral, thermal, x-ray diffraction and DNA interaction with Pd (ii), Cu(ii), and Cd (ii) of hydrazone derivatives. *Appl. Organomet. Chem.* **2021**, *35*, e6153. [CrossRef]
34. Deljoo, M. The molecular dynamics study of CO<sub>2</sub>, SO<sub>2</sub>, and NO<sub>2</sub> pollution capture from O<sub>2</sub> environment via polyether/polyamide-Ag membranes. *Preprint* **2024**. [CrossRef]
35. Addicoat, M.; Vankova, N.; Akter, I.; Heine, T. Extension of the universal force field to metal–organic frameworks. *J. Chem. Theory Computation* **2014**, *10*, 880–891. [CrossRef] [PubMed]
36. Jaillet, L.; Artemova, S.; Redon, S. Im-uff: Extending the universal force field for interactive molecular modeling. *J. Mol. Graph. Model.* **2017**, *77*, 350–362. [CrossRef] [PubMed]
37. Tokarský, J.; Čapkova, P.; Burda, J. Structure and stability of kaolinite/TiO<sub>2</sub> nanocomposite: DFT and MM computations. *J. Mol. Model.* **2011**, *18*, 2689–2698. [CrossRef] [PubMed]
38. Chen, Y.; Wang, Y.; Huang, L.; Su, B.; Yang, Y. Investigating the microscopic mechanism of ultrasonic-vibration-assisted-pressing of WC-co powder by simulation. *Materials* **2023**, *16*, 5199. [CrossRef] [PubMed]
39. Wang, W.; Pan, Y.; Zhang, W.; Liu, X.; Li, L. The size effect to O<sup>2-</sup>–Ce<sup>4+</sup> charge transfer emission and band gap structure of Sr<sub>2</sub>CeO<sub>4</sub>. *Luminescence* **2018**, *33*, 907–912. [CrossRef]
40. Goldsby, J. Basic elastic properties predictions of cubic cerium oxide using first-principles methods. *J. Ceramics* **2013**, *1*, 323018. [CrossRef]
41. Tagne, A.; Simo-Tagne, M.; Kharchi, R.; Ndukwu, M.; Assoumani, N.; Compaoré, A.; Zoulalian, A. Numerical study of the pyrolysis of wood chips for biocharcoal production: Influence of chips geometry and initial moisture content. *Energies* **2022**, *15*, 4098. [CrossRef]
42. Gamero-Barraza, J.I.; Pámanes-Carrasco, G.A.; Delgado, E.; Cabrales-Arellano, C.P.; Medrano-Roldán, H.; Gallegos-Ibáñez, D.; Wedwitschka, H.; Reyes-Jáquez, D. Computational modelling of extrusion process temperatures on the interactions between black soldier fly larvae protein and corn flour starch. *Food Chem. Molecular Sci.* **2024**, *8*, 100202. [CrossRef]
43. Zhuravlev, Y.N.; Obolonskaya, O.S. Structure, mechanical stability, and chemical bond in alkali metal oxides. *J. Struct. Chem.* **2010**, *51*, 1005–1013. [CrossRef]
44. David, W.I.F.; Jones, M.O.; Gregory, D.H.; Jewell, C.M.; Johnson, S.R.; Walton, A.; Edwards, P.P. A mechanism for non-stoichiometry in the lithium amide/lithium imide hydrogen storage reaction. *J. Am. Chem. Soc.* **2007**, *129*, 1594–1601. [CrossRef]
45. Annamareddy, A.; Eapen, J. Ion hopping and Constrained Li diffusion pathways in the superionic state of antiperovskite Li<sub>2</sub>O. *Entropy* **2017**, *19*, 227. [CrossRef]
46. Yuan, P.; Liu, B.; Sun, H. Optimization of the crystallization process of bis(2-hydroxyethyl) terephthalate. *Cryst. Res. Technol.* **2021**, *56*, 2100025. [CrossRef]
47. Song, L.; Bediako, J.; Song, M.; Kim, J.; Cho, C.; Zhao, Y.; Choi, J. Effective recovery of Pt(IV) from acidic solution by a defective metal-organic frameworks using central composite design for synthesis. *Sustain. Chem. Eng.* **2019**, *7*, 7510–7518. [CrossRef]
48. Moustafa, I.; Mohamed, N.; Ibrahim, S. Molecular modeling and antimicrobial screening studies on some 3-aminopyridine transition metal complexes. *Open J. Inorg. Chem.* **2022**, *12*, 39–56. [CrossRef]
49. Nagappayya, S.; Gaikar, V.; Ali, S. Designing of ligands for solvent extraction of Cs<sup>+</sup> using molecular modeling approach. *Desalination Water Treat.* **2012**, *38*, 1–7. [CrossRef]
50. Orekhov, M. Coordination numbers of bivalent ions in organic solvents. *Russ. J. Phys. Chem. A* **2021**, *95*, 2059–2064. [CrossRef]
51. Rodríguez, I.; Valladares, R.; Hinojosa-Romero, D.; Valladares, A. Emergence of magnetism in bulk amorphous palladium. *Phys. Rev. B* **2019**, *100*, 024422. [CrossRef]

- 
52. Liu, X.; Du, J.; Hua, L.; Liu, K. First-principles comparative study of CuFeSe<sub>2</sub> and CuFeS<sub>2</sub>. *Mater. Res.* **2023**, *26*, e20220371. [[CrossRef](#)]
  53. Yu, Y.; Chen, S.; Li, X.; Zhu, J.; Liang, H.; Zhang, X.; Shu, Q. Molecular dynamics simulations for 5,5'-bistetrazole-1,1'-diolate (TKX-50) and its PBXs. *RSC Adv.* **2016**, *6*, 20034–20041. [[CrossRef](#)]

**Disclaimer/Publisher's Note:** The statements, opinions and data contained in all publications are solely those of the individual author(s) and contributor(s) and not of MDPI and/or the editor(s). MDPI and/or the editor(s) disclaim responsibility for any injury to people or property resulting from any ideas, methods, instructions or products referred to in the content.